RSC Advances

PAPER

Cite this: *RSC Adv.*, 2019, **9**, 33814

Electrodeposited Pd/graphene/ZnO/nickel foam electrode for the hydrogen evolution reaction

Na Wang,†[a] Bairui Tao, †*[a] Fengjuan Miao *[a] and Yu Zang[b]

Received 12th July 2019
Accepted 3rd October 2019

DOI: 10.1039/c9ra05335b

rsc.li/rsc-advances

Efficient electrocatalysts are crucial to water splitting for renewable energy generation. In this work, electrocatalytic hydrogen evolution from Pd nanoparticle-modified graphene nanosheets loaded on ZnO nanowires on nickel foam was studied in an alkaline electrolyte. The high electron mobility stems from the cylindrical ZnO nanowires and the rough surface on the graphene/ZnO nanowires increases the specific surface area and electrical conductivity. The catalytic activity arising from adsorption and desorption of intermediate hydrogen atoms by Pd nanoparticles improves the hydrogen evolution reaction efficiency. As a hydrogen evolution reaction (HER) catalyst, the Pd/graphene/ZnO/Ni foam (Pd/G/ZnO/NF) nanocomposite exhibits good stability and superior electrocatalytic activity. Linear sweep voltammetry (LSV) revealed an overpotential of −31 mV and Tafel slope of 46.5 mV dec^{-1} in 1 M KOH. The economical, high-performance, and environmentally friendly materials have excellent prospects in hydrogen storage and hydrogen production.

1. Introduction

Hydrogen plays an important role in renewable energy due to the large combustion heat (287 kJ mol^{-1}) and environmental friendliness.[1] The hydrogen evolution reaction (HER) is an important step in water splitting to produce hydrogen[2] and efficient catalysts are crucial. Among the various types of metallic catalysts, platinum (Pt) delivers the best performance due to the nearly zero overpotential but it is expensive and has limited abundance. Alternative elements such as Pd with excellent catalytic capability and hydrogen storage have been proposed. For instance, bimetallic structure like Pd/Ag (ref. 3) and Pd/Pt (ref. 4) or composites of Pd and metallic or nonmetallic oxides (Pd/graphene,[5] Pd/MoS_2,[6] and Pd/ZnO[7]) can improve chemisorption of hydrogen atoms on the electrode surface.

Among the non-metallic catalytic materials for the HER, carbon-based materials such as carbon black, carbon nanotubes, and graphene have aroused interest.[8–10] Especially, graphene has good mechanical strength, large specific surface area, and high electrical and thermal conductivity[11,12] and many strategies have been proposed to synthesize the proper nanoarchitectures to improve the catalytic efficiency. It has been shown that the electrocatalytic performance is affected by the specific surface area[13] and metal catalysts fabricated on n-doped graphene have better durability and electrocatalytic activity. ZnO is an n-type wide-bandgap semiconductor with high electron mobility as well as excellent optical, electronic and photocatalytic properties.[14] Therefore, the graphene/ZnO hybrid may have large potential from the viewpoint of the hydrogen evolution reaction.

In this work, the Pd/graphene/ZnO/Ni foam (Pd/G/ZnO/NF) nanocomposite was fabricated by a hydrothermal method and electroplating and the HER activity was evaluated. The ZnO nanowires on the Ni foam provide high electron mobility to facilitate hydrogen evolution and graphene nanosheets improve the electrical conductivity and specific surface area.

2. Experimental details

2.1 Materials and reagents

The Ni foam (thickness of 0.5 mm, pore density of 110 PPI, and areal density of 420 g m^{-2}) was purchased from Suzhou Qiandingli Electronic Technology Co. Ltd. and graphene slurry (5 wt%) was obtained from Suzhou Graphene Nanotechnology Co. Ltd. Palladium chloride ($PdCl_2$), ammonium chloride (NH_4Cl), ammonia ($NH_3 \cdot H_2O$), zinc acetate ($Zn(CH_3COO)_2$), zinc nitrate hexahydrate ($Zn(NO_3)_2 \cdot 6H_2O$), and hexamethylene tetramine (HMTA) were acquired from Sinopharm Chemical Reagent Co. Ltd. (China). All the reagents were analytical grade and used without further purification. The solutions were prepared with deionized (DI) water.

2.2 Preparation of ZnO/Ni foam, G/Ni foam, and G/ZnO/Ni foam

Four different composite electrodes, namely NF, G/NF, ZnO/NF, and G/ZnO/NF were fabricated. The square Ni foam (1 cm × 1

[a]College of Communications and Electronics Engineering, Qiqihar University, Heilongjiang 161006, China. E-mail: tbr_sir@163.com; miaofengjuan@163.com; Fax: +86-452-2738748; Tel: +86-452-2742787

[b]College of Materials Science and Engineering, Qiqihar University, Wenhua Street 42, Qiqihar, China

† Na Wang and Bairui Tao are co-first authors.

cm) was cleaned in acetone, HCl, and ethanol, immersed in a solution containing 0.1 M zinc acetate [$Zn(CH_3COO)_2$] for 3 min, and annealed at 200 °C for 30 min to form ZnO seed layers. In the hydrothermal process, 50 mM $Zn(NO_3)_2 \cdot 6H_2O$ and 50 mM HMTA were dissolved in deionized (DI) water. The ZnO-seeded NF was placed in the precursor solution at 95 °C for 5 h and then annealed at 300 °C for 1 h to produce ZnO-coated NF (labeled as ZnO/NF). Afterwards, 1 mL of the oily slurry of graphene was dispersed in 10 mL of ethanol by mild sonication to form solution A. NF and ZnO/NF were put into solution A under stirring for 2 min and dried at 60 °C to produce graphene-coated NF (labeled as G/NF) and graphene-coated ZnO/NF (labeled as G/ZnO/NF).

2.3 Preparation of palladium nanoparticles coated electrodes

Electrochemical plating was adopted to produce the Pd/NF, Pd/ZnO/NF, Pd/G/NF, and Pd/G/ZnO/NF electrodes. The solution for palladium plating contained 2.7 mM $PdCl_2$, 0.35 M NH_4Cl, and an appropriate amount of $NH_3 \cdot H_2O$ was added to adjust the pH to 8–9. The electrodes and platinum were the cathode and anode, respectively, during electroplating in the palladium plating solution. The current density was at 10 mA cm^{-2} and electroplating time was 30 min. The electrodes were removed, cleaned with deionized water, and dried for 30 min at 60 °C to produce Pd/NF, Pd/ZnO/NF, Pd/G/NF, and Pd/G/ZnO/NF. The schematic diagram of Pd/G/ZnO/NF electrode formation is shown in Fig. 1, and the steps of other electrode formation can be removed accordingly.

2.4 Apparatus and measurement procedures

The morphology and microstructure of the electrodes were characterized by scanning electron microscopy (FE-SEM, Hitachi S-4800) and Field-emission transmission electron microscope (TEM/HRTEM, JEM 2100F), energy-dispersive X-ray spectroscopy (EDS Type GENESIS 60) and the crystal structure the chemical states was investigated by X-ray diffraction (XRD, Rigaku, RINT2000, Cu $K_{\alpha 1}$ radiation, $\lambda = 0.154$ nm) and X-ray photoelectron spectroscopy (XPS, ESCALAB250Xi). Elemental composition was determined by the inductively coupled plasma mass-spectrometer (ICP-MS, Elan DRC II PerkinElmer SCIEX). The electrochemical tests were carried out on the CHI660D electrochemical workstation (Shanghai Chenhua CHI660D) in the three-electrode mode. The fabricated electrodes served as the working electrodes, whereas the saturated calomel electrode (SCE) and platinum electrode were the reference and counter electrodes, respectively. The electrochemical properties were determined by cyclic voltammetry (CV), linear sweep voltammetry (LSV), and electrochemical impedance spectroscopy (EIS). The CV data were obtained in the potential window between −1.4 and 0.6 V *vs.* SCE at scanning rates from 10 to 100 mV s^{-1}. EIS was conducted at the open circuit potential with a 5 mV perturbation amplitude and the frequency range was from 10^5 to 10^{-1} Hz. The electrochemical measurements were performed in 1 M KOH at room temperature (25 °C).

3. Results and discussion

3.1 Structural characterization

The surface morphology of Pd/NF, ZnO/NF, G/ZnO/NF and Pd/G/ZnO/NF was examined by scanning electron microscopy (SEM) as shown in Fig. 2. The macroporous topography of the Pd/G/ZnO/NF electrode is shown in Fig. 2a, where a layer of fluffy, porous material is clearly visible on the surface of the nickel foam. The microstructure of the fabricated Pd/NF composite is a dense layer of Pd nanoparticles attached to the nickel foam, while the size of the Pd nanoparticles is 40–80 nm (Fig. 2b). It can be clearly seen that some Pd nanoparticles agglomerate. There are needle-like ZnO nanowires uniformly distributed on the nickel foam according to Fig. 2c and a higher-magnification SEM image (inset of Fig. 2c) further revealed the specific surface area of the electrode can be enhanced by the needle-like structure of ZnO. Fig. 2d depicts the SEM image of G/ZnO/NF electrode. Graphene sheets whose size is about 2 μm can be clearly observed on the surface of ZnO nanowires. Fig. 2e and f show different magnification SEM diagrams of Pd/G/ZnO/NF electrode. In Fig. 2d and f, it can be seen that large multilayer graphene nanosheets are unevenly distributed and agglomerated due to dip preparation.

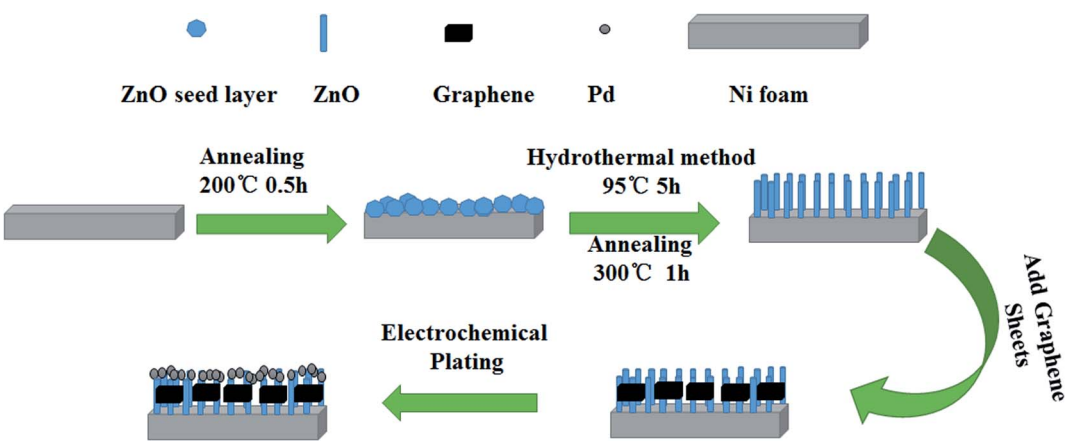

Fig. 1 The schematic depiction of Pd/G/ZnO/NF electrode formation.

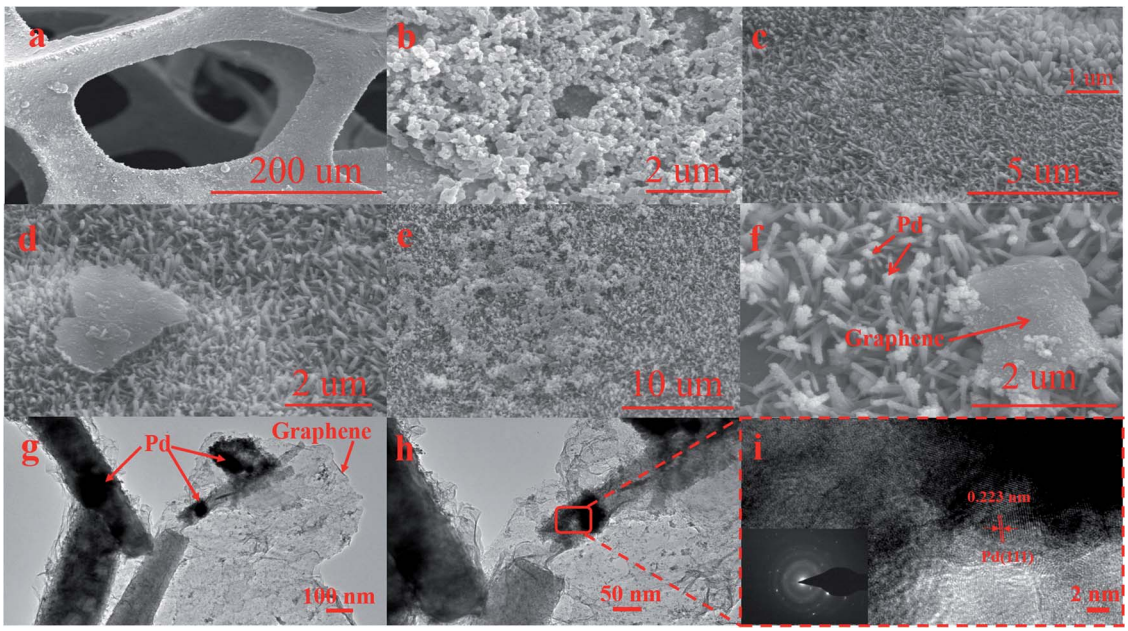

Fig. 2 (a) and (b) SEM images of Pd/G/ZnO/NF and Pd/NF, (c) SEM images of ZnO/NF and inset is higher magnification SEM image of ZnO/NF, (d) SEM image of G/ZnO/NF, (e) and (f) SEM images of Pd/G/ZnO/NF with different magnification, (g) and (h) TEM images of Pd/G/ZnO/NF, (i) HRTEM image of Pd/G/ZnO/NF, inset is SAED of Pd/G/ZnO/NF.

As shown in Fig. 2e (a higher-magnification SEM image of Fig. 2a), Pd nanoparticles were evenly deposited on the surface of G/ZnO/NF with some cracks and gaps. Bumps and hollows were observed that Pd nanoparticles were partly on graphene sheets and partly on the top of ZnO nanowires with larger magnification (Fig. 2f), suggesting an increased specific surface area of the electrode after the electrodeposition of Pd. Moreover, Pd nanoparticles distribution on the electrode were more uniform than that in Pd/NF (Fig. 2b), which was attributed to the acicular structure of ZnO. Growth of Pd nanoparticles on graphene nanowires and ZnO nanowires was confirmed by Transmission electron microscopy (TEM) and High resolution TEM (HRTEM) for Pd/G/ZnO/NF (Fig. 2g–i). The TEM images in Fig. 2g and h show the diameter of the Pd nanoparticles is 40–80 nm and the morphology of Pd nanoparticles is spherical. HRTEM showed the lattice fringe of 0.223 nm, consistent with the Pd (111) plane (Fig. 2i). The selected area electron diffraction (SAED) pattern (inset of Fig. 2i) shows a clear polycrystalline structure.

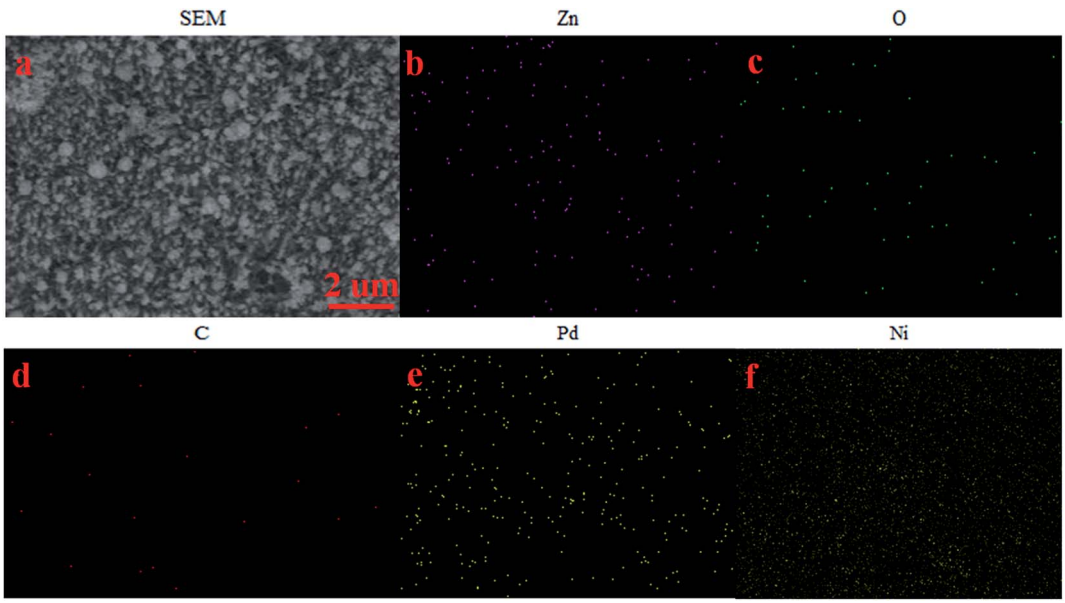

Fig. 3 (a) SEM image, (b–f) corresponding EDS mapping of the Pd/G/ZnO/NF electrode.

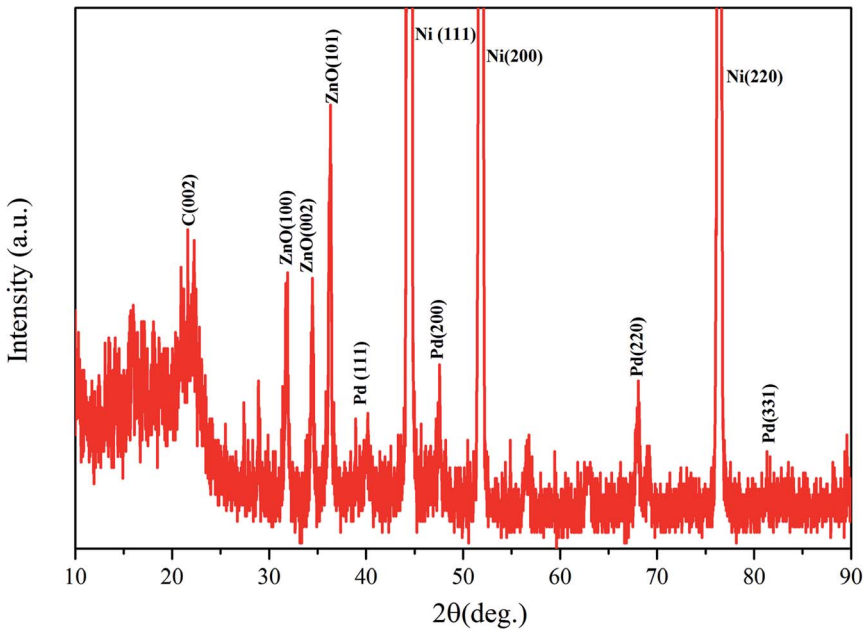

Fig. 4 XRD spectrum of Pd/G/ZnO/NF.

Fig. 3 investigate the element distribution of the Pd/G/ZnO/NF electrode by EDS mapping. Fig. 3a shows SEM micrographs of the microstructural features in the Pd/G/ZnO/NF electrode, and corresponding EDS mapping was shown in Fig. 3b–f, thus disclosing the presence of Zn, O, Ni, C, and Pd elements. Fig. 3d shows a small amount of element C due to the small amount of graphene added.

The crystal structure of the Pd/G/ZnO/NF electrode is characterized by XRD as shown in Fig. 4. The peaks of the face-

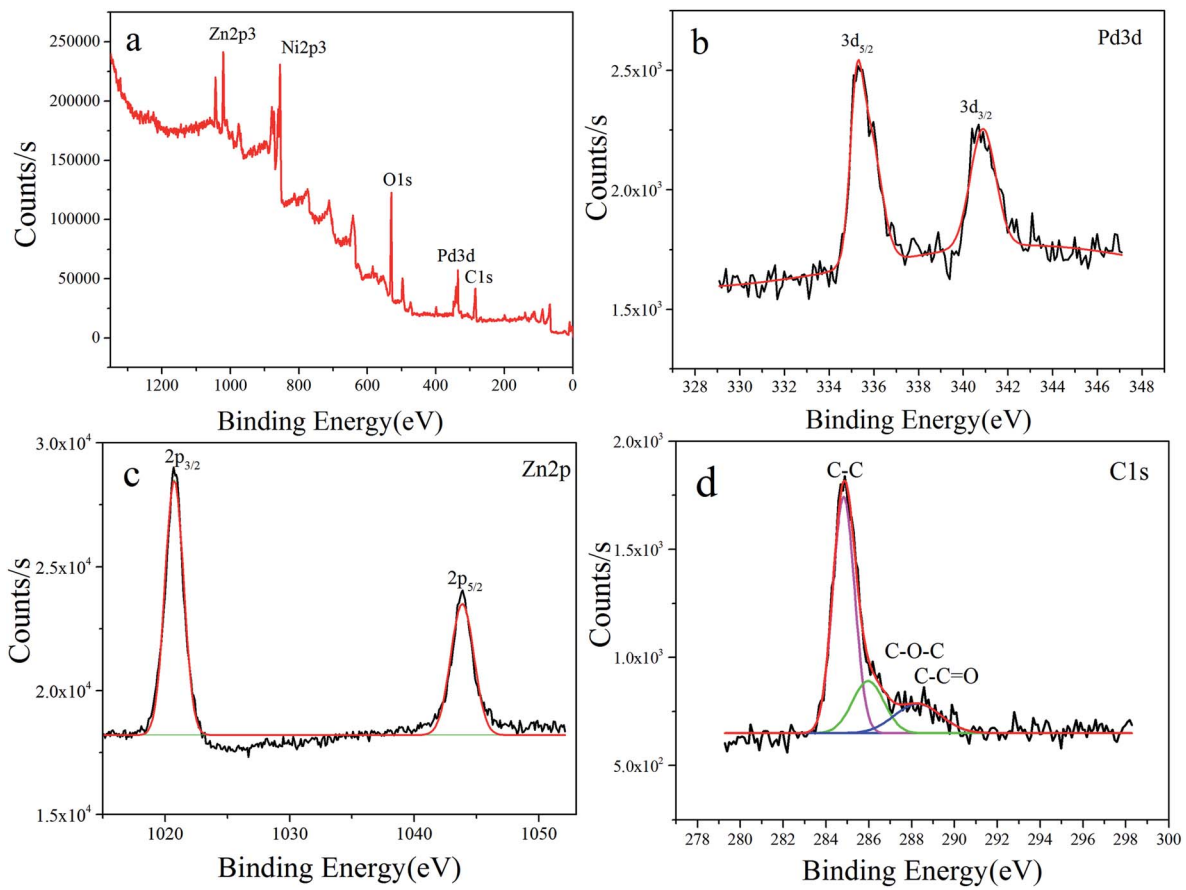

Fig. 5 (a) XPS spectrum of Pd/G/ZnO/NF, (b) XPS spectrum of Pd, (c) XPS spectrum of ZnO, and (d) XPS spectrum of graphene.

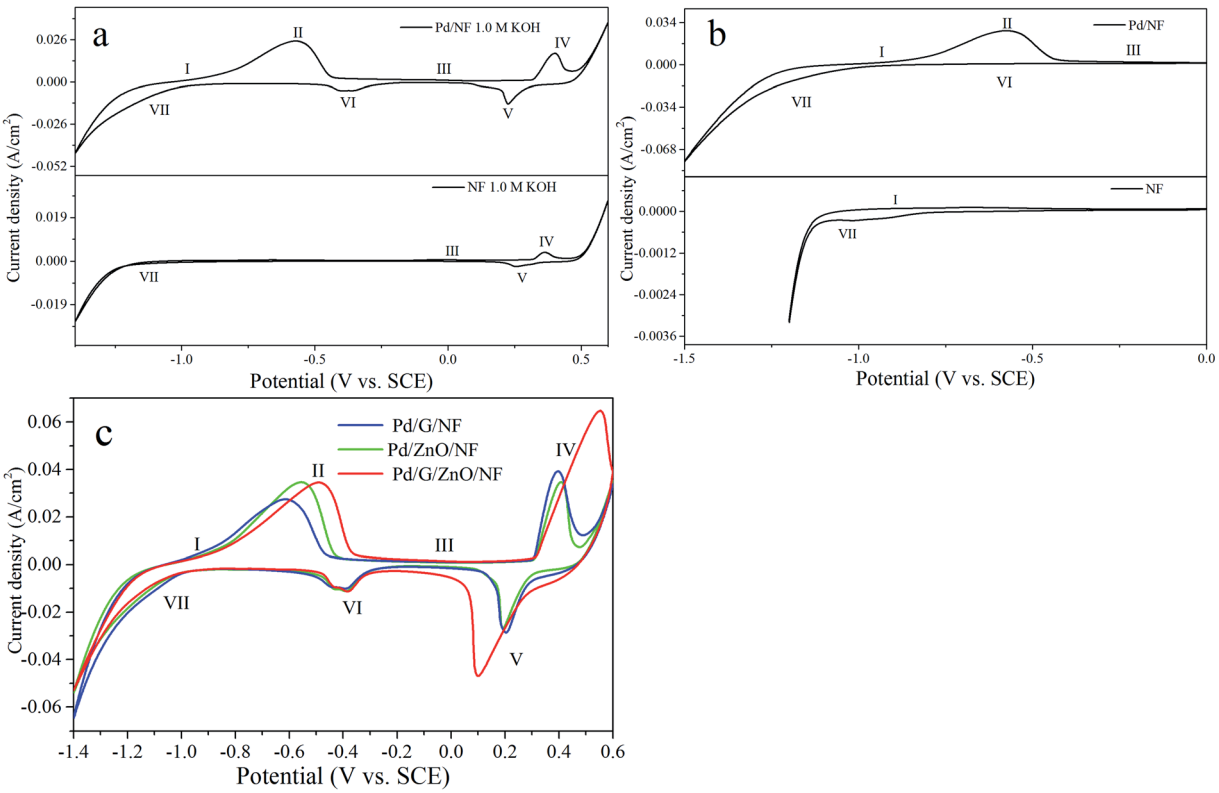

Fig. 6 (a) CV of NF and Pd/NF in the potential region between −1.4 and 0.6 V *vs.* SCE, (b) CV of NF and Pd/NF in the related negative potential region between −1.5 and 0 V *vs.* SCE, (c) CV of Pd/G/NF, Pd/ZnO/NF, and Pd/G/ZnO/NF in the potential region between −1.4 and 0.6 V *vs.* SCE at a scanning rate 10 mV s^{-1}.

centered cubic structure at 44.6°, 51.6° and 76.3° can be assigned to (111), (200) and (220) planes of the nickel substrate, respectively. The face-centered cubic Pd metal shows characteristic peaks at $2\theta = 40.1°$, 46.3°, 68.3°, and 81.8° corresponding to the (111), (200), (220), and (311) planes. The other diffraction peak at 21.6° is the characteristic peak of graphene. The presence of the graphene peak at this location may be due to its oxidation and reduction in the air. The three diffraction peaks at 31.9°, 34.2°, and 36.3° correspond to the (100), (002), and (101) planes of the ZnO nanowires array, respectively.

XPS analysis was carried out to understand the surface chemical state of Pd/G/ZnO/NF electrode. Fig. 5a shows Ni, Pd, Zn, O, and C originating from the Ni foam substrate, graphene, ZnO, and Pd. Fig. 5b shows that the binding energies of the major spin–orbit split doublet (Pd $3d_{5/2}$ and Pd $3d_{3/2}$) of Pd/G/ZnO/NF are 335.3 eV and 340.7 eV, respectively, in good agreement with metallic Pd(0).[7] Fig. 5c shows that the peaks of Zn 2p have binding energies of 1020.73 eV and 1043.85 eV attributed to Zn $2p_{3/2}$ and Zn $2p_{1/2}$ corresponding to Zn(II) in ZnO. The C 1s spectrum in Fig. 5d can be fitted with three peaks at 284.8 eV, 286.5 eV, and 288 eV related to C–C, C–O–C, and C–C=O, respectively, consistent with the literature.[5] The peak of C1 indicates that the graphene part has been oxidized.

3.2 Cyclic voltammetry characterization of Pd/G/ZnO/NF

Fig. 6a shows that cyclic voltammograms (CV) were obtained from the Pd/NF and NF electrodes in the potential range between −1.4 and 0.6 V *vs.* SCE at a scanning rate of 10 mV s^{-1}. It can be seen that a number of redox peaks are attributed to different electrochemical processes occurring at the surface of the electrode. The CV curves in the potential range between −1.5 and 0 V *vs.* SCE are showed in Fig. 6b. The shape of the voltammograms is the same for all cycles (between 1^{st} and 50^{th}) and only the peak current changes during the potential sweep. In case of NF electrode (the bottom side of Fig. 6a and b), peak I at the potential range between −0.8 and −0.7 V *vs.* SCE is appeared owing to the formation of α-$Ni(OH)_2$ (eqn (1)) during the first positive potential scan. Peak III appeared from 0 to 0.1 V *vs.* SCE originates from the transformation of α-$Ni(OH)_2$ → β-$Ni(OH)_2$ species (eqn (2)). With the potential moving to more positive values, a pair of redox peaks (IV and V) are ushered in, which are the mutual transformation of β-$Ni(OH)_2$ and β-NiOOH (eqn (3) and (4)). In the potential range between −1.1 and −1 V *vs.* SCE, the cathodic peak VII is a reduced process of β-$Ni(OH)_2$ (eqn (5)). The corresponding voltammetric results can be described by the following reactions:

$$Ni + 2OH^- \rightarrow \alpha\text{-}Ni(OH)_2 + 2e^- \quad (1)$$

$$\alpha\text{-}Ni(OH)_2 + nNi + 2nOH^- \rightarrow (n+1)\beta\text{-}Ni(OH)_2 + 2ne^- \quad (2)$$

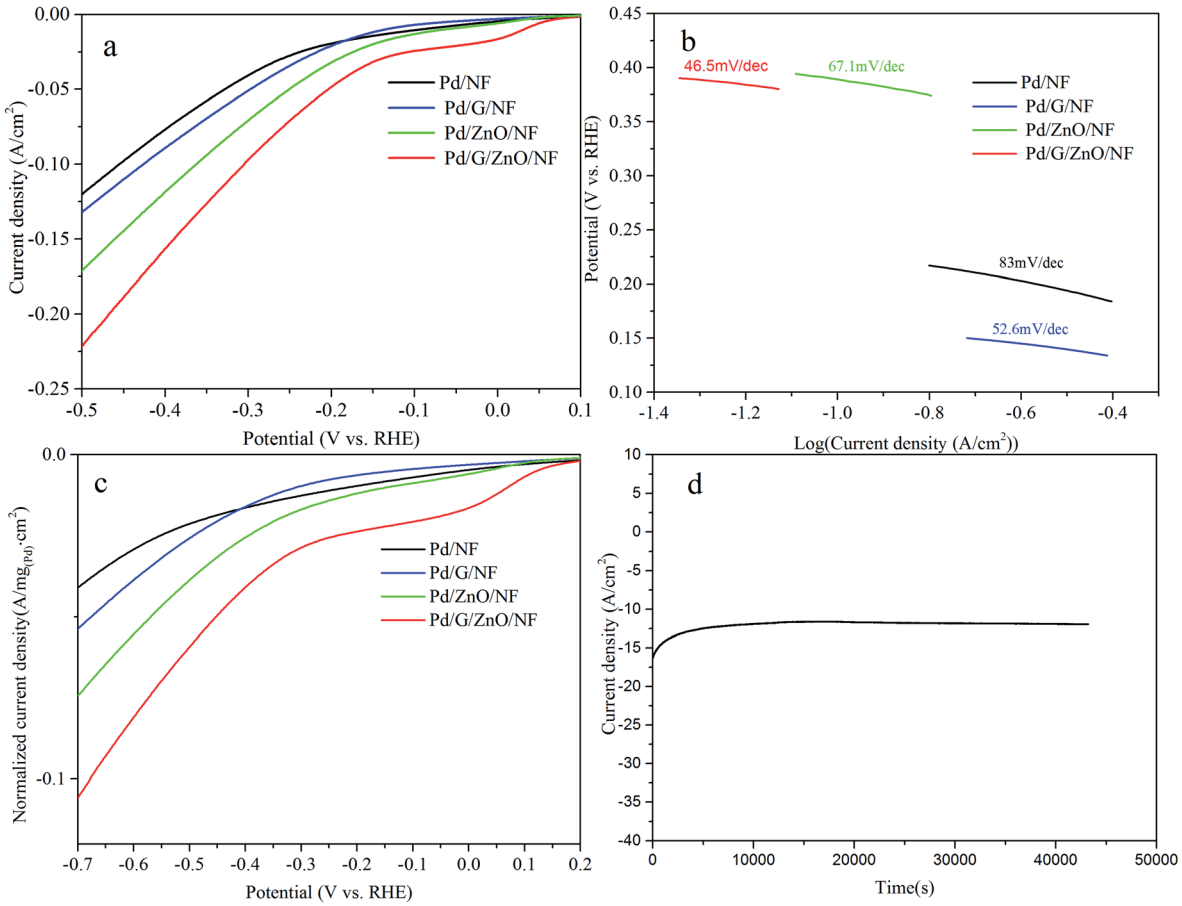

Fig. 7 (a) LSV polarization curve of Pd/NF, Pd/G/NF, Pd/ZnO/NF, and Pd/G/ZnO/NF at a scanning rate of 10 mV s^{-1} and (b) corresponding Tafel plots, (c) the LSV of the catalysts with normalized current density by Pd mass, (d) chronoamperometric curves (I–t) of Pd/G/ZnO/NF.

$$\beta\text{-Ni(OH)}_2 + OH^- \rightarrow \beta\text{-NiOOH} + H_2O + e^- \quad (3)$$

$$\beta\text{-NiOOH} + H_2O + e^- \rightarrow \beta\text{-Ni(OH)}_2 + OH^- \quad (4)$$

$$\beta\text{-Ni(OH)}_2 + 2e^- \rightarrow Ni + 2OH^- \quad (5)$$

$$PdH + OH^- \rightarrow H_2O + Pd + e^- \quad (6)$$

$$Pd + 2OH^- \rightarrow PdO + H_2O + 2e^- \quad (7)$$

$$PdO + H_2O + 2e^- \rightarrow Pd + 2OH^- \quad (8)$$

$$Pd + H_2O + e^- \rightarrow PdH + OH^- \quad (9)$$

For the Pd/NF electrode (Fig. 6a), it is no need to repeat the explanation of the same reaction mechanism as the NF electrode. According to eqn (6), an anode peak II at potential of approximately −0.65 V *vs.* SCE is appeared owing to the desorption of diffusional hydrogen absorbed in Pd nanoparticles' lattice interstices. The oxide state of palladium (PdO) (eqn (7)) appears at peak III, which overlapping with the electrochemical transformation process of α-$Ni(OH)_2$ into β-$Ni(OH)_2$. Peak VI originates from the reaction in which PdO is reduced to Pd (eqn (8)) while peak VII which starts from −1.4 to −1 V *vs.* SCE can be attributed to the hydrogen absorption process (eqn (9)) on the surface of Pd nanoparticles which overlapping with the reduced process of β-$Ni(OH)_2$. As shown in Fig. 6b, owning to the absence of oxidation state of Pd at the limited upper potential, the reduction peak of PdO disappears during the decreasing potential scans.

Fig. 6c compares the cyclic voltammetry (CV) curves of Pd/G/NF, Pd/ZnO/NF, and Pd/G/ZnO/NF in the potential range of −1.4 to 0.6 V *vs.* SCE at a scanning rate of 10 mV s^{-1}. The same CV shape is observed from the electrodes in this potential range. In these CV curves, the adsorption/absorbed hydrogen peak current of the NF is weakest in all electrodes obviously while the hydrogen peak current of the other three electrodes (Pd/G/NF, Pd/ZnO/NF, Pd/G/ZnO/NF) are almost identical. It can be said that no hydrogen evolution reaction took place on the surface of the NF electrode. For the peak II, the highest peak current density of Pd/G/ZnO/NF results from the higher electrochemical activity because of the large surface area of ZnO and high conductivity of graphene.

Fig. 7a shows linear sweep voltammetry (LSV) obtained from Pd/NF, Pd/G/NF, Pd/ZnO/NF, and Pd/G/ZnO/NF) in 1 M KOH at a scanning rate of 10 mV s^{-1} and Fig. 7b shows the

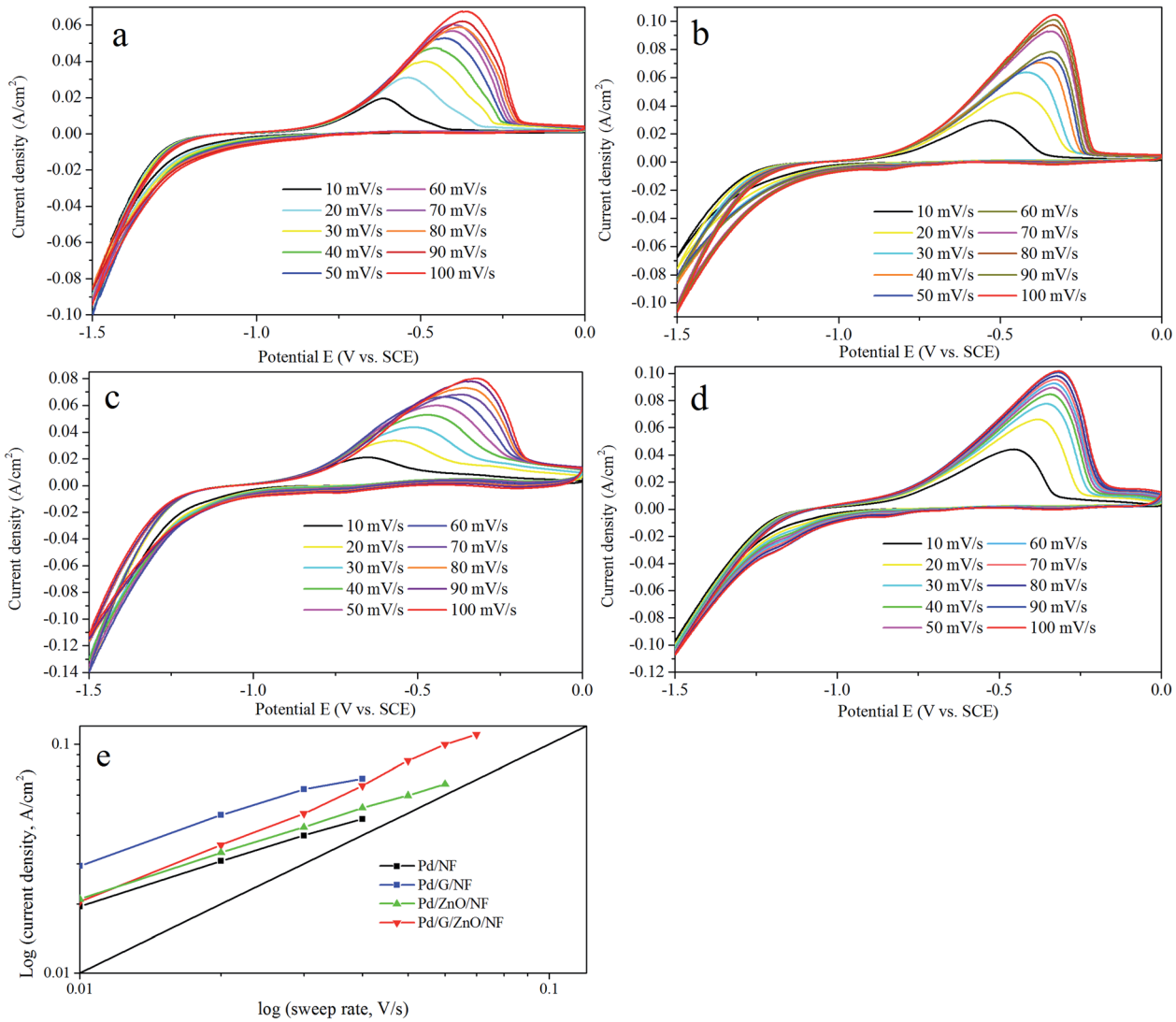

Fig. 8 CV of (a) Pd/NF, (b) Pd/G/NF, (c) Pd/G/ZnO/NF, and (d) Pd/G/ZnO/NF in the potential range between −1.5 and 0 V *vs.* SCE for different scanning rates in 1 M KOH; (e) relationship between the anodic peak current densities and scanning rates for different samples.

corresponding Tafel plots. The LSV and Tafel data are shown in the reversible hydrogen electrode (RHE) potential for simplicity.[15] Therefore, the zero of overpotential can be determined at 1.067 V *vs.* SEC due to the electrochemical test are done in 1 M KOH solution (pH ∼ 14). More importantly, overpotential is an important indicator of hydrogen evolution

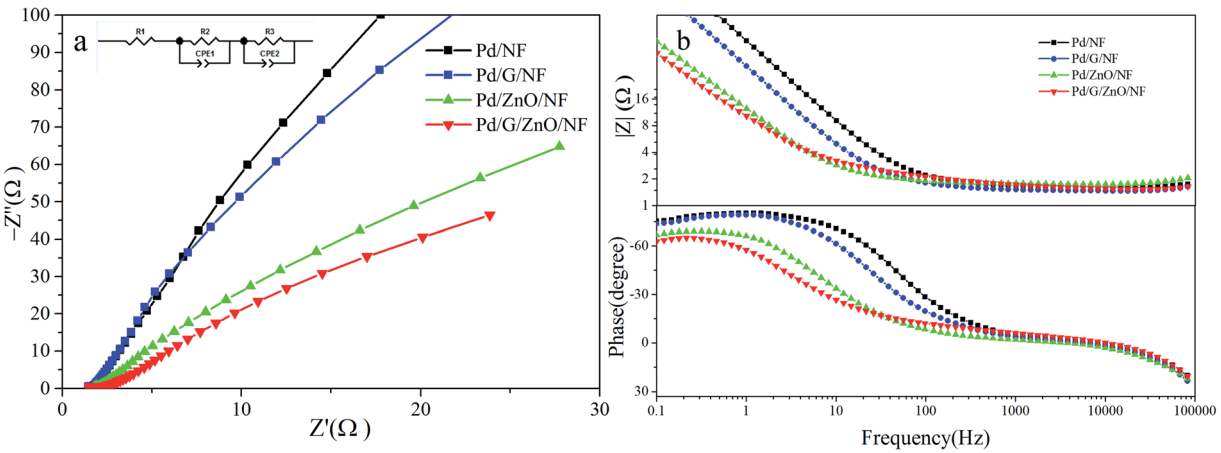

Fig. 9 (a) Nyquist and (b) Bode plots of Pd/NF, Pd/G/NF, Pd/ZnO/NF, and the inset of (a) the equivalent circuit diagram of Pd/G/ZnO/NF.

ability, that is, the smaller the overpotential, the better the hydrogen evolution performance. The overpotentials of Pd/NF, Pd/G/NF, Pd/ZnO/NF, and Pd/G/ZnO/NF) are, respectively, −125 mV, −91 mV, −80 mV, and −31 mV at a cathodic current density of 10 mA cm^{-2} and the overpotential of Pd/G/ZnO/NF is the smallest. At a large cathodic current density such as 100 mA cm^{-2}, the overpotential of Pd/G/ZnO/NF is −306 mV that is smaller than those of Pd/ZnO/NF (−363 mV), Pd/G/NF (−427 mV), and Pd/NF (−427 mV) again showing Pd/G/ZnO/NF has the highest electrocatalytic activity. The corresponding Tafel slope is obtained by fitting the linear region in the LSV curve to the Tafel equation. The Tafel slope of Pd/G/ZnO/NF (46.5 mV dec^{-1}) is smaller than those of the other electrocatalysts for Pd/NF (83 mV dec^{-1}), Pd/G/NF (52.6 mV dec^{-1}), and Pd/ZnO/NF (67.1 mV dec^{-1}). The Tafel slope is in good agreement with the LSV data confirming the good HER characteristics of Pd/G/ZnO/NF. The content of Pd in the four electrodes was investigated by ICP-MS. The loading mass of Pd nanoparticles on the Pd/G/ZnO/NF electrode was 0.45 mg (0.45 mg cm^{-2}), which was similar to that of the Pd/ZnO/NF electrode 0.44 mg (0.44 mg cm^{-2}), the Pd/G/NF electrode 0.44 mg (0.44 mg cm^{-2}) and the Pd/NF electrode 0.43 mg (0.43 mg cm^{-2}), respectively. Fig. 7c exhibits the LSV of the catalysts with normalized current density by the loading Pd mass. The Pd/G/ZnO/NF shows much higher normalized current density than others at the same potential, the results are good for hydrogen evolution reaction. Fig. 7d shows the stability test of Pd/G/ZnO/NF electrode at overpotential 0.4 V for 12 hours. The change of current density is normal at the beginning, possibly without deaeration of the electrode or the reduction of oxide on the electrode surface. The current density after initial period remained stable, which proved the excellent stability of the Pd/G/ZnO/NF electrode.

Fig. 8a–d show the electrochemical properties of Pd/NF, Pd/G/NF, Pd/ZnO/NF, and Pd/G/ZnO/NF are examined between −1.5 and 0 V *vs.* SCE at scanning rates between 10 and 100 mV s^{-1} in 1 M KOH. Oxidation–reduction of Pd nanoparticles is avoided by selecting the upper limit potential 0 V *vs.* SCE. The samples yield similar cyclic voltammograms and show the oxidation–reduction behavior in this potential region. There are two anodic peaks associated with the formation of passive α-$Ni(OH)_2$ amorphous layer (I) and oxidation of adsorbed hydrogen on the Pd nanoparticles (II). However, it is almost impossible to see peak I and the reduction peak of PdO disappears during the decreasing potential scans due to the absence of oxidation state of Pd in the limited upper potential. The reduction peak (VII) increases gradually according to Fig. 8a–d. As the electrochemical rate increases, oxidation of adsorbed hydrogen on the Pd nanoparticles corresponding to the fully anodic peaks (II) even at the large sweep rate is improved. It can be concluded that the combination of ZnO, graphene, and Pd facilitates hydrogen evolution.

Fig. 8e shows that the current densities of anodic peak II (j, with the unit of A cm^{-2}) change with the sweeping rates ν (V s^{-1}) as the plot of log(j) *versus* log(ν). Moreover, there is a line with a slope of 1 for comparison. The transfer coefficient is close to 1 for the Pd/G/ZnO/NF electrode for sweeping rates from 10 to 100 mV s^{-1} because oxidation of adsorbed hydrogen on the Pd surface is a surface-controlled process.[16] The slopes of Pd/NF, Pd/G/NF, and Pd/ZnO/NF are 0.6, 0.64, and 0.7 respectively, which are smaller than that of Pd/G/ZnO/NF, indicative of the high resistance.

3.3 Impedance measurements

Electrochemical impedance spectroscopy (EIS) which is a powerful technique to study the electrode kinetics in HER[17,18] is performed on Pd/NF, Pd/G/NF, and Pd/ZnO/NF and Pd/G/ZnO/NF in the range of 10^5 to 10^{-1} Hz at the open circuit potential with an AC excitation signal of 5 mV in 1 M KOH. Fig. 9a and b show the impedance diagrams as plots of Nyquist and Bode planes. The electrochemical resistance of the hydrogen reduction reaction on Pd/G/ZnO/NF is less than that on the other electrodes and the electrochemical impedance of Pd/NF is the biggest. The Pd/G/ZnO/NF electrode is smaller than the other electrodes as shown in Fig. 9b. The results reveal that the HER activity is markedly improved by incorporating ZnO and graphene into Pd/NF. The inset of Fig. 9a presents the equivalent circuit and the fitting equivalent circuit is consistent with the experimental data. LSV is an important parameter to measure the effects of the hydrogen evolution reaction. The properties of Pd-based catalysts in the literature are compared in Table 1 which shows that the overpotential of Pd/G/ZnO/NF is the smallest (31 mV) among the five electrodes at a current density is 10 mA cm^{-2}. The Tafel slope (46.5 mV dec^{-1}) of Pd/G/ZnO/NF is the smallest among these electrodes. Therefore, Pd/G/ZnO/NF electrode has excellent hydrogen evolution performance, and the preparation method is simple, economical, and eco-friendly.

Table 1 Comparison of HER activity of Pd/G/ZnO/NF with other catalysts

Working electrode	Tafel slope (mV dec^{-1})	Overpotential/current density (mV)/(mA cm^{-2})	Ref.
Pd/G/ZnO/NF	46.5	31/10	This work
rGO-$Au_{48}Pd_{52}$	149	130/10	8
Pd_xCu_{100-x}/C	48	102/10	9
$Pd_{17}Se_{15}$	57	182/10	15
$PdBi_2$	63	78/10	18

4. Conclusion

Pd nanoparticles are electrodeposited on graphene-coated ZnO on Ni foam. Cyclic voltammetry, Tafel plots, and electrochemical impedance spectroscopy are performed to determine the HER properties in 1 M KOH. The Pd/G/ZnO/NF electrode shows high conductivity and stability by cyclic voltammetry in addition to enhanced electrocatalytic hydrogen evolution as indicated by an overpotential of 31 mV and Tafel slope of 46.5 mV dec^{-1} at 10 mA cm^{-2}. Our results disclose that Pd/G/ZnO/NF has outstanding catalytic activity and stability in HER rendering it promising in hydrogen production.

Conflicts of interest

There are no conflicts to declare.

Acknowledgements

We would like to thank the technology Innovation Center of Agricultural Multi-Dimensional Sensor Information Perception, Heilongjiang Province. This work was jointly supported by the University Nursing Program for Young Scholars with Creative Talents in Heilongjiang Province (Grant No. UNPYSCT-2016087), Scientific Research Foundation for the Returned Overseas Chinese Scholars in Heilongjiang Province, Project of Plant food Processing Technology-Heilongjiang Province superiority and characteristic discipline (Grant No. YSTSXK201873), Fundamental Research Funds in Heilongjiang Provincial Universities (No. 135109244, 135309115, 135309211).

References

1 Z. Guoqiang, L. Yue and R. Kun, Epitaxial Growth of $Ni(OH)_2$ Nanoclusters on MoS_2 Nanosheets for Enhanced Alkaline Hydrogen Evolution Reaction, *Nanoscale*, 2018, **10**(40), 19074–19081.

2 X. Chen, K. Yu and Y. Shen, Synergistic Effect of MoS_2 Nanosheets and VS_2 for Hydrogen Evolution Reaction with Enhanced Humidity Sensing Performance, *ACS Appl. Mater. Interfaces*, 2017, **9**(48), 42139–42148.

3 P. S. Toth, M. Velicky and T. J. A. Slater, Hydrogen evolution and capacitance behavior of Au/Pd nanoparticle-decorated graphene heterostructures, *Applied Materials Today*, 2017, **8**, 125–131.

4 B. Rezaei, M. Mokhtarianpour and A. A. Ensafi, Hydrogen evolution reaction and formic acid oxidation by decorated nanostructural Pt/Pd on a copper-filled nanoporous stainless steel, *J. Iran. Chem. Soc.*, 2018, **15**(4), 955–965.

5 S. Ghasemi, S. R. Hosseini and S. Nabipour, Palladium nanoparticles supported on graphene as an efficient electrocatalyst for hydrogen evolution reaction, *Int. J. Hydrogen Energy*, 2015, **40**(46), 16184–16191.

6 B. B. Li, S. Z. Qiao and X. R. Zheng, Pd coated MoS_2 nanoflowers for highly efficient hydrogen evolution reaction under irradiation, *J. Power Sources*, 2015, **284**, 68–76.

7 B. Li, R. Wang and X. Shao, Synergistically enhanced photocatalysis from plasmonics and a co-catalyst in Au@ZnO–Pd ternary core–shell nanostructures, *Inorg. Chem. Front.*, 2017, **4**(12), 2088–2096.

8 J. A. S. B. Cardoso, L. Amaral and Ö. Metin, Reduced graphene oxide assembled Pd-based nanoalloys for hydrogen evolution reaction, *Int. J. Hydrogen Energy*, 2017, **42**(7), 3916–3925.

9 X. Zhang, D. Wu and D. Cheng, Component-dependent electrocatalytic activity of PdCu bimetallic nanoparticles for hydrogen evolution reaction, *Electrochim. Acta*, 2017, **246**, 572–579.

10 Z. Sun, X. Wei and H. Shen, Preparation and evaluation of Pd/polymeric pyrrole-sodium lauryl sulfonate/foam-Ni electrode for 2,4-dichlorophenol dechlorination in aqueous solution, *Electrochim. Acta*, 2014, **129**, 433–440.

11 Y. Koskun, A. Savk and B. Sen, Highly sensitive glucose sensor based on monodisperse palladium nickel/activated carbon nanocomposites, *Anal. Chim. Acta*, 2018, **1010**, 37–43.

12 H. Tian, H. Fan and J. Ma, Noble metal-free modified electrode of exfoliated graphitic carbon nitride/ZnO nanosheets for highly efficient hydrogen peroxide sensing, *Electrochim. Acta*, 2017, **247**, 787–794.

13 C. Tang, N. Cheng and Z. Pu, NiSe Nanowire Film Supported on Nickel Foam: An Efficient and Stable 3D Bifunctional Electrode for Full Water Splitting, *Angew. Chem.*, 2015, **127**(32), 9483–9487.

14 S. Masudy-Panah, Y. J. K. Eugene and N. D. Khiavi, Aluminum-incorporated p-CuO/n-ZnO photocathode coated with nanocrystal-engineered TiO_2 protective layer for photoelectrochemical water splitting and hydrogen generation, *J. Mater. Chem. A*, 2018, **6**(25), 11951–11965.

15 S. Kukunuri, P. M. Austeria and S. Sampath, Electrically Conducting Palladium Selenide (Pd_4Se, $Pd_{17}Se_{15}$, Pd_7Se_4) Phases: Synthesis and Activity Towards Hydrogen Evolution Reaction, *Chem. Commun.*, 2016, **52**, 206–209.

16 M. Anand Raj and S. Arumainathan, Comparative Study of Hydrogen Evolution Behavior of Nickel Cobalt and Nickel Cobalt Magnesium Alloy Film Prepared by Pulsed Electrodeposition, *Vacuum*, 2018, **160**, 461–466.

17 C. Hu, Y. Tian and J. Wang, Structural evolution and optical properties of hydrogenated germanium carbonitride films, *Vacuum*, 2016, **129**, 23–30.

18 F. Li, J. Li and X. Lin, Designed synthesis of multi-walled carbon nanotubes@Cu@MoS_2 hybrid as advanced electrocatalyst for highly efficient hydrogen evolution reaction, *J. Power Sources*, 2015, **300**, 301–308.

